

NEUTRON AND X-RAY SPECTROSCOPY

Françoise HIPPERT

*Laboratoire des Matériaux et du Génie Physique
Institut National Polytechnique, Grenoble*

Erik GEISSLER

*Laboratoire de Spectrométrie Physique
Université Joseph Fourier, Grenoble*

Jean-Louis HODEAU

Laboratoire de Cristallographie, CNRS, Grenoble

Eddy LELIÈVRE-BERNA

Institut Laue-Langevin, Grenoble

Jean-René REGNARD

*Département de Recherche Fondamentale sur la Matière Condensée
CEA-Grenoble, Université Joseph Fourier, Grenoble*



Springer

2005

Grenoble Sciences

Grenoble Sciences pursues a triple aim :

- ◆ to publish works responding to a clearly defined project, with no curriculum or vogue constraints,
- ◆ to guarantee the selected titles' scientific and pedagogical qualities,
- ◆ to propose books at an affordable price to the widest scope of readers.

Each project is selected with the help of anonymous referees, followed by a one-year (in average) interaction between the authors and a Readership Committee, whose members' names figure in the front pages of the book. Publication is then confided to the most adequate publishing company by Grenoble Sciences.

(Contact: Tél.: (33) 4 76 51 46 95 – Fax: (33) 4 76 51 45 79

E-mail: Grenoble.Sciences@ujf-grenoble.fr)

Scientific Director of Grenoble Sciences : Jean BORNAREL,
Professor at the Joseph Fourier University, Grenoble 1, France

Grenoble Sciences is supported by the French Ministry of Education and Research and the “Région Rhône-Alpes”.

Front cover photo: harmonious composition based on figures extracted from the work:

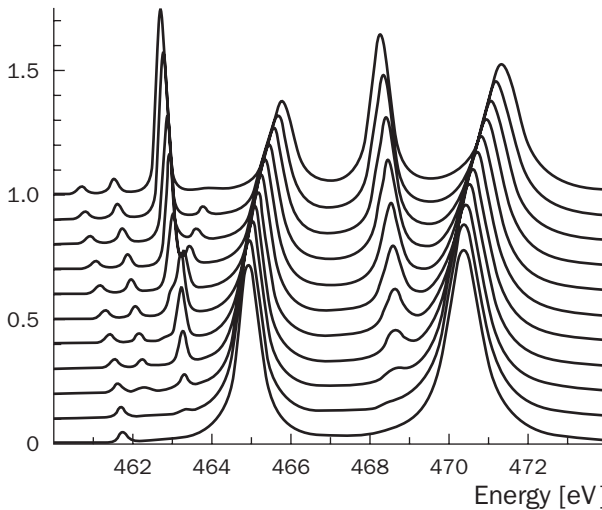
- ◆ The body-centred tetragonal unit cell of the bilayer manganite by CURRAT (after ref. [38])
- ◆ Methyl group in lithium acetate dihydrate and in aspirin by JOHNSON (from refs [19] and [49])
- ◆ X-PEEM images of permalloy micro-structures and of carbon films by SCHNEIDER (from ref. [11] and taken from ref. [17])
- ◆ Interference of outgoing and backscattered photoelectron wave by LENGELER.

EXTRAITS

Table 25 - The T_1 final states of the $2p^5 3d^1$ configuration with $10 Dq = 3.04$ eV. The top row gives the energies of the seven final states that are build from seven basis vectors. The third row is related to 1P_1 character and is given in boldface.

	460.828	461.641	462.806	464.048	465.859	468.313	471.369
$J = 1$	0.0662	0.0037	0.1550	0.0124	0.4916	0.0404	0.2308
$J = 1$	0.5944	0.0253	0.0007	0.2972	0.0280	0.0078	0.0466
$J = 1$ 1P_1	0.0046^a	0.0091^b	0.1128^c	0.0046^d	0.1845^e	0.2666^f	0.4178^g
$J = 3$	0.0161	0.4460	0.0340	0.0980	0.0097	0.2923	0.1039
$J = 3$	0.0020	0.2973	0.2980	0.0791	0.0331	0.2191	0.0714
$J = 3$	0.0044	0.0404	0.3986	0.0116	0.2417	0.1738	0.1294
$J = 4$	0.3124	0.1781	0.0009	0.4972	0.0113	0.0000	0.0001

Figure 13 shows the crystal field multiplet calculations for the $3d^0 \rightarrow 2p^5 3d^1$ transition in Ti^{IV} . The result of each calculation is a set of seven energies with seven intensities. These seven states are broadened by the lifetime broadening and the experimental resolution. From a detailed comparison to experiment it turns out to be the case that each of the four main lines has to be broadened differently. It is well known that the L_{II} part of the spectrum (i.e. the last two peaks) contains an additional Auger decay that accounts for a significant broadening with respect to



the L_{III} part. This effect has been found to be an additional broadening of 0.5 eV half-width at half-maximum (hwhm) [27,28].

Figure 13 - Crystal field multiplet calculations for the $3d^0 \rightarrow 2p^5 3d^1$ transition in Ti^{4+} . The atomic Slater-Condon parameters and spin-orbit couplings have been used as given in table 12. The bottom spectrum is the atomic multiplet spectrum. Each next spectrum has a value of $10 Dq$ that has been increased by 0.3 eV. The top spectrum has a crystal field of 3.0 eV.

3.3. COMPLEX HEDIN-LUNDQVIST EXCHANGE AND CORRELATION POTENTIAL

We shall not fully develop the formalism of the complex Hedin-Lundqvist potential and we shall concentrate on its specific importance for the simulation of X-ray absorption cross-sections. The potential felt by the photoelectron in the single-electron approach contains a mean part, an exchange part and what is left receives the name of correlation potential. Expressions for the exchange and correlation parts have been developed by Hedin and Lundqvist [28] as a by-product of the calculation of the self-energy of the photoelectron. The self-energy contains all the interactions of the photoelectron with the other electrons of the medium. It is a complex function where the real part is the sum of the exchange and correlation energy and the imaginary part is a damping term representing the inelastic interactions of the photoelectron with the medium. The medium is simulated by a dielectric function, usually defined in the plasmon pole approximation and the interaction of the photoelectron with the medium is expressed as a series of the screened interaction. Only the first term is computed (this is the so called GW approximation). When the photoelectron kinetic energy is larger than the plasmon energy of the valence electrons (that is the plasmon energy associated with the electronic density in the interstitial region), the photoelectron is undergoing severe inelastic losses. This corresponds to a sharp increase of the imaginary part of the photoelectron self-energy. Following a simple model derived from the WKB procedure, one can relate the imaginary part of the photoelectron self-energy ($\Im\Sigma$) in the atomic spheres or in the interstitial region to an estimation of the photoelectron mean free path $\lambda_{el}(E)$, as a function of the kinetic energy, E , of the photoelectron.

$$\lambda_{el}(E) = \frac{\hbar^2 k}{2m} \frac{1}{\Im\Sigma}$$

One sees (fig. 4) that below the plasmon energy (here it is ≈ 9 eV, $\lambda_{el}(E)$ is infinite.

If one considers also the finite life time of the core-hole, one can calculate an effective mean free path for a specific edge. It is given by

$$\lambda_{eff} = \frac{\hbar}{\Gamma_{tot}(E)} \sqrt{\frac{2E}{m}}$$

with

$$\Gamma_{tot}(E) = \Gamma_h + \Gamma_{el} (+\Gamma_{exp})$$

where Γ_h is the core-hole width and Γ_{el} is the damping function related to the photoelectron mean free path $\lambda_{el}(E)$, $\Gamma_{el} = \frac{\hbar}{\lambda_{el}(E)} \sqrt{\frac{2E}{m}}$. An eventual Γ_{exp} term can

The challenge in the theoretical development is to describe the final state $|f\rangle$ correctly. This is quite easy for the case of transitions to a localized state within the multiplet framework, and represents the most important application of XMCD. More challenging are transitions toward delocalized states (itinerant magnetism). The former is extensively described in the chapter by J. Vogel and F. de Groot in this volume. The greatest impact of XMCD in the field of thin film and interfacial magnetism is given special attention in the chapter by C.M. Schneider. Here, we limit ourselves to the underlying basis of the XMCD effect and comments on the theoretical approach of XMCD for the itinerant magnetism case.

2.2. LIGHT POLARIZATION AND POLARIZATION-DEPENDENT SELECTION RULES

The interaction Hamiltonian depends on the polarization $\boldsymbol{\varepsilon}$ of the incident electric field.

- ◆ **Linear polarization:** The electromagnetic field vector has a constant direction in a plane perpendicular to the propagation vector.
- ◆ **Circular polarization:** The electromagnetic field vector rotates around the propagation vector direction (fig. 1).

The selection rules are polarization-dependent, i.e., the difference between the transition probability for left and right circularly polarized light gives circular magnetic dichroism:

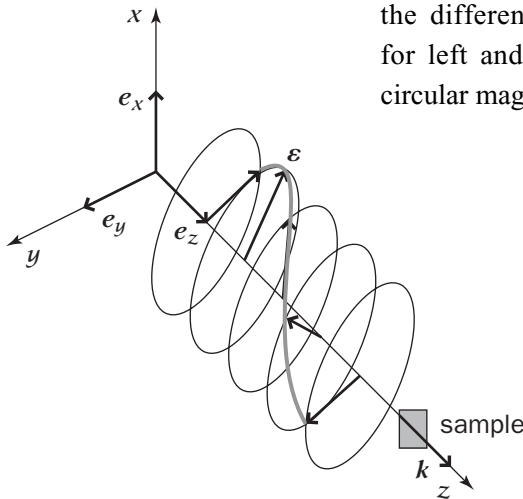


Figure 1 - Circular polarization: the electromagnetic field vector turns around the direction of the propagation vector. In the figure the X-rays are left circularly polarized, the electromagnetic field turns to the left for an observer placed at the sample position.

For a left circularly polarized beam propagating along Oz, the expression for the electric field is

$$\boldsymbol{\varepsilon}^+ = \frac{\mathbf{e}_x + i\mathbf{e}_y}{\sqrt{2}}$$

Finally the experimental signal is proportional to

$$XMCD = \frac{\sigma_+ - \sigma_-}{\sigma_+ + \sigma_-} = \frac{\alpha' - \alpha}{\alpha' + \alpha} \frac{\rho\uparrow - \rho\downarrow}{\rho\uparrow + \rho\downarrow} = \frac{1}{2} P_e \cdot P_c \cdot \frac{\Delta\rho}{\rho}$$

with $\alpha^+_{\uparrow} = \alpha^-_{\downarrow} = \alpha'$ and $\alpha^+_{\downarrow} = \alpha^-_{\uparrow} = \alpha$ (see remarks, section 2.3.2)

$$P_e = \frac{\alpha' - \alpha}{\alpha' + \alpha} \quad \text{and} \quad \frac{\Delta\rho}{\rho} = \frac{\rho\uparrow - \rho\downarrow}{\rho\uparrow + \rho\downarrow}$$

where the degree of circular polarization of the X-ray photons is accounted for by the factor P_c .

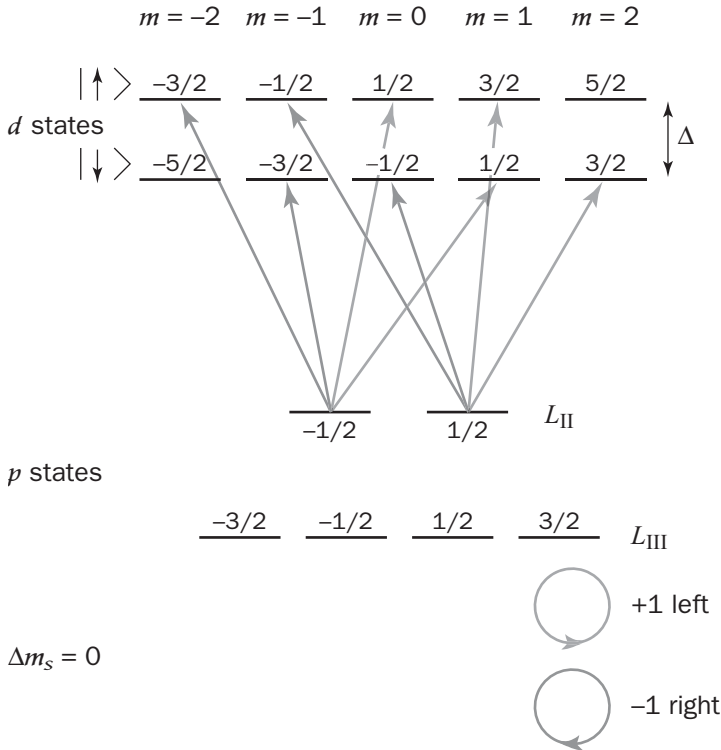


Figure 2 - For an L_{II} edge, Dipole transitions from a $J = 1/2$ level for photons of helicity +1 (left polarization, $\Delta m_I = +1$), for linearly polarized photons ($\Delta m_I = 0$) and for photons of helicity -1 (right polarization, $\Delta m_I = -1$). The p level is split by spin-orbit coupling interaction. The d level is split by exchange interaction Δ .

2.3.2. CALCULATION OF P_e FOR THE L_{II} AND L_{III} EDGES: $P_e(L_{II})$ AND $P_e(L_{III})$

Due to spin-orbit coupling the $2p$ band is split into two sub-bands of kinetic moment $j = 1/2$ and $j = 3/2$. This is a final state effect. The two sublevels can be separated by energy as large as 1000 eV in the case of 5d transition metals or in rare earths.

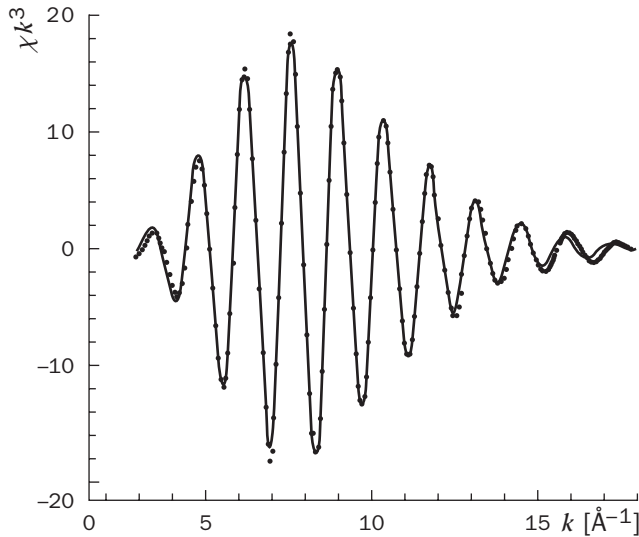


Figure 12 - Fit of the first shell Cu data at room temperature with the first shell Cu data measured at 77 K.

It is not always possible to separate the different shells by a window function. For instance, in a bcc metal the first and second neighbour are located at $a\sqrt{3}/2$ and at a . The difference is only 13% and the corresponding shells merge into one. In such a case a two-shell fit has to be used. Now the question arises how many free parameter may be determined in a significant way by the fit. The answer is given by the ratio of the window width Δr_F and the resolution in Fourier space $(k_{\max} - k_{\min})^{-1}$

$$N_{\text{free}} \leq \frac{2}{\pi} \Delta r_F (k_{\max} - k_{\min}) \quad \{44\}$$

For the data in figure 12, $\Delta r_F = 0.8 \text{ \AA}$ and $k_{\max} - k_{\min} = 15 \text{ \AA}^{-1}$, so that $N_{\text{free}} \leq 8$. Since not every good-looking fit is a significant fit, equation {44} is an important criterion in data analysis.

3.5. POSITION AND STRUCTURE OF THE ABSORPTION EDGE

Figure 13 shows the K edge of Cu in three Cu oxides (Cu_2O , CuO and KCuO_2), in metallic copper and in a high T_c superconductor $\text{YBa}_2\text{Cu}_3\text{O}_{6.97}$. There are distinct differences in the form and in the position of the edges. It turns out that the position of the edge is shifted to higher energies with increasing formal valence of the absorber. Note that $\tilde{\mu}$ is the absorption coefficient normalized to an edge jump of 1 (for above relative to far below the edge).

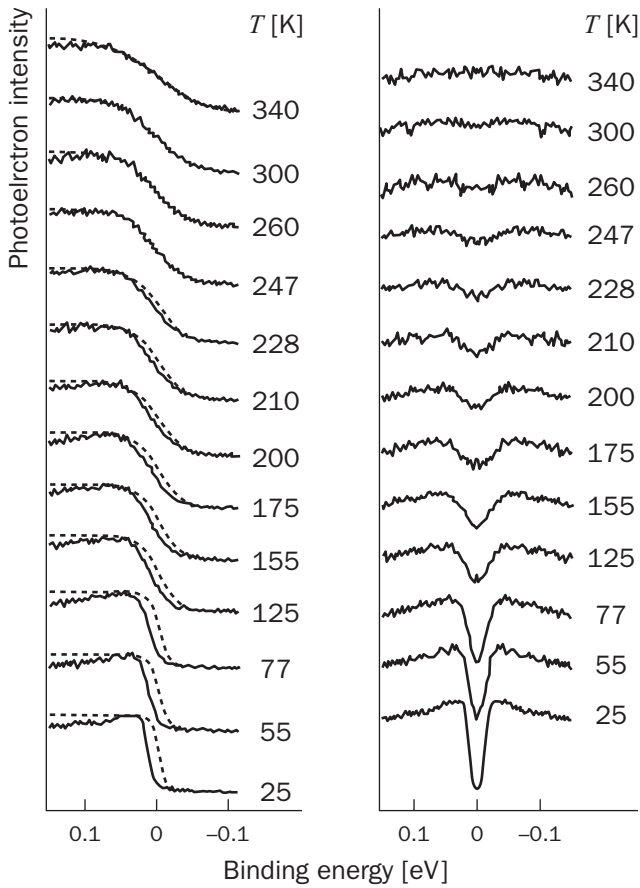


Figure 22 - Temperature-dependent raw (left) and symmetrized spectra of a C_{60} monolayer on the Ag(100) surface, showing the opening of a gap at E_F from ref. [25].

Perfect nesting of the FS, i.e. the possibility of translating the entire FS onto itself by a translation $\Delta k = Q_{CDW} = 2k_F$, is at the origin of the instability. The degeneracy of states at the Fermi surface connected by Q_{CDW} causes the divergence of the generalized charge susceptibility $\chi(2k_F)$ and, *via* electron-phonon coupling, the spontaneous charge and lattice modulation. Perfect nesting cannot be achieved in 2D or 3D, except for pathological situations, like a square FS. Nevertheless, partial nesting conditions over a good portion of the FS are often realized in quasi-2D materials, like the layered transition metal compounds. The ensuing enhancement of $\chi(2k_F)$ may be sufficient to drive the system into a CDW phase. Unlike the singular 1D situation, partial nesting removes only part – the nested portion – of the FS, and the transition is not a metal to insulator, but a metal-to-metal one.

Both 1D and 2D instabilities, and the corresponding changes in electronic states, have been studied by ARPES. The "geometrically" simpler 1D case presents some

5.1.2. CONTRAST ENHANCEMENT

In order to separate magnetic and nonmagnetic contributions to the contrast in the EEM image, one conveniently uses the fact that a reversal of ζ changes the sign of the magneto-dichroic signal C_M , while leaving the nonmagnetic signal C_{NM} essentially unaffected, i.e.,

$$C_M(-\zeta) = -C_M(\zeta) \quad ; \quad C_{NM}(-\zeta) = C_{NM}(\zeta) \quad \{1\}$$

Therefore, by subtracting two images taken at the same photon energy, but opposite light helicity $I_{\zeta^+} - I_{\zeta^-}$, the magnetic contrast C_M is enhanced. Summing up the two images extracts the non-magnetic contrast C_{NM}

$$C_M \sim I_{\zeta^+} - I_{\zeta^-} \quad ; \quad C_{NM} \sim I_{\zeta^+} + I_{\zeta^-} \quad \{2\}$$

This way, the images provide both magnetic and nonmagnetic (chemical, topographical) information. In order to describe the magnetic contrast in a more quantitative manner, often the *asymmetry* image A

$$A = \frac{I_{\zeta^+} - I_{\zeta^-}}{I_{\zeta^+} + I_{\zeta^-}} \quad \{3\}$$

rather than the difference image C_M is shown. The quantity asymmetry ranges between +100% and -100%.

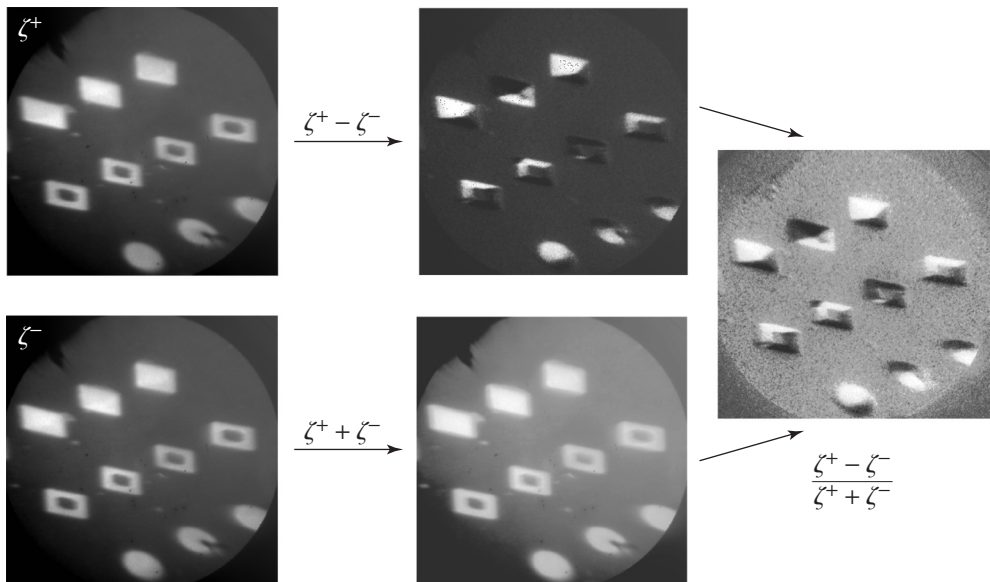


Figure 8 - Magnetic contrast enhancement for the example of permalloy microstructures. Feature size is 12 nm. **Left** - Individual images taken with opposite light helicity $I(\zeta^+)$ and $I(\zeta^-)$ at the Ni L_{III} edge are first subtracted and summed (**center**), respectively. **Right** - The sum and difference images are finally used to calculate an asymmetry image. See also ref. [11].

In an inelastic neutron scattering experiment, one measures the number of neutrons scattered from a sample as a function of their final wave vector k_f given their initial wave vector k_i . The scattering event is thus characterized by 6 variables: three components of k_i and three components of k_f . However, what we are really interested in is the energy transfer $\hbar\omega$ and momentum (or wave vector) transfer \mathbf{Q} from the neutron to the sample, given by the energy and momentum conservation rules,

$$\hbar\omega = E_i - E_f = \frac{\hbar^2}{2m}(k_i^2 - k_f^2) \quad \{1\}$$

and
$$\mathbf{Q} = \mathbf{k}_i - \mathbf{k}_f \quad \{2\}$$

respectively. This corresponds to only four variables, i.e. there are two redundant variables, which should be carefully chosen to optimize the experiment. For non-crystalline samples, only $Q = |\mathbf{Q}|$ and $\hbar\omega$ are meaningful, and there are four redundant variables.

2.2. SCATTERING TRIANGLE

It is useful to study the diagram in real (fig. 1a) and reciprocal (fig. 1b) space of a scattering event. The latter is called the scattering triangle, and shows the kinematical conditions k_i and k_f must fulfil to obtain a particular energy and momentum transfer; one talks about "closing the scattering triangle". From figure 1b, it is easily seen that for a given $\hbar\omega$ and \mathbf{Q} , any combination of k_i and k_f that lies on the dotted line in the figure can be chosen. This corresponds to one of the two redundant variables in the scattering event mentioned above. It is used to optimize the intensity and resolution of the experiment, as discussed in the following chapters.

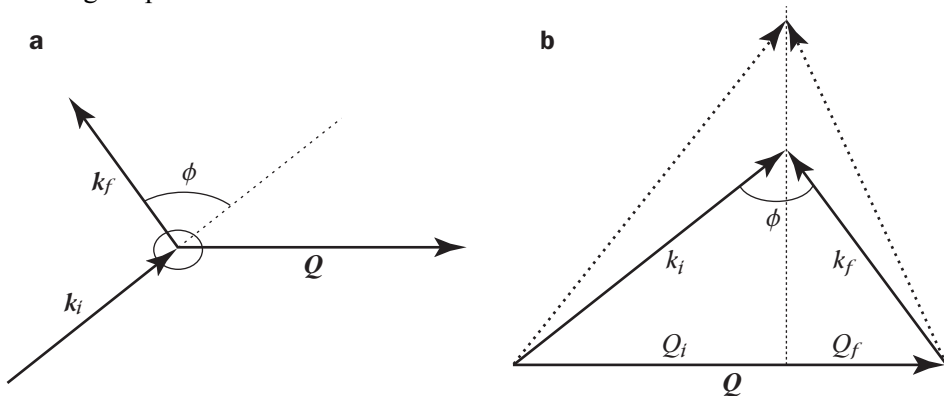


Figure 1 - Scattering event in (a) real space and (b) reciprocal space Q_i and Q_f are the projections of k_i and k_f onto Q and ϕ is the scattering angle.

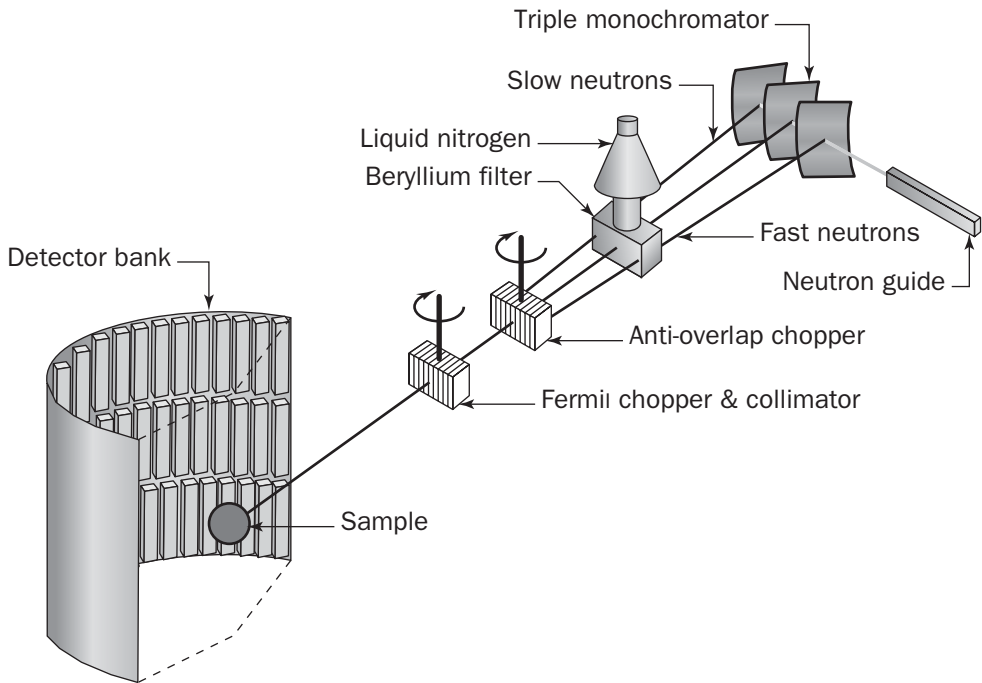


Figure 8 - The IN6 spectrometer at the ILL.

IN4, also at the ILL, uses a large focussing crystal monochromator to select the incident energy with a Fermi chopper to provide the pulse structure^[9]. The focussing of the monochromator provides a large flux enhancement for experiments where beam divergence and consequently Q resolution is less important. The curvature of the monochromator can be carefully controlled to provide optimal space and time focussing conditions^[10].

Two background choppers are used to eliminate fast neutrons and γ s and produce broad pulses that are then incident on the monochromator. The Fermi chopper is located between the monochromator and the sample.

TOF instruments on a steady state source have an advantage over instruments on a pulsed source in that their maximum operating frequency is not dictated by the source. However, innovative instrumentation designs may provide the opportunity to increase the effective repetition rate on a pulsed source by phasing an array of chopper in such a way that the pulse can effectively be used several times.

4.3. MULTI-CHOPPER TOF SPECTROMETERS

I will refer to the last group of chopper spectrometers as multi-chopper TOF instruments. There are several examples on steady state sources, such as NEAT at

The Hamiltonian is solved in terms of products of two-dimensional oscillator functions and one-dimensional rotator functions.

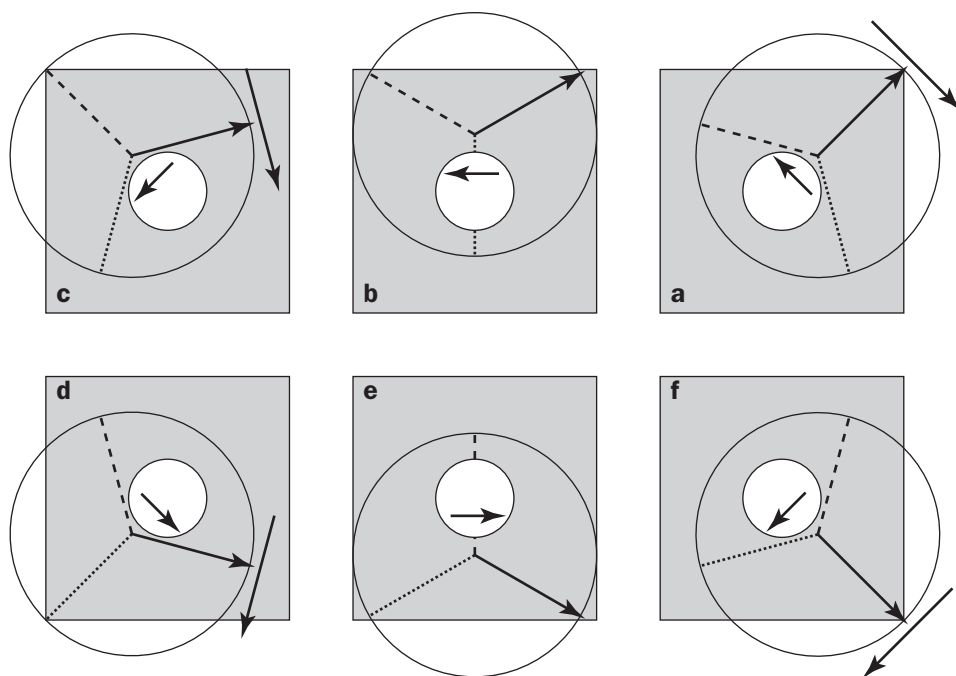


Figure 2 - Schematic representation of rotation-translation coupled dynamics. The centre of mass traces out a complete period in the anti-clockwise direction (**a-f-a**), while the protons undergo a reorientation of $2\pi/3$ in the opposite sense. Quantum mechanically, the central atom of the rotor occupies a larger volume than in SPM and the proton distribution is approximately square.

The above Hamiltonians refer to molecular systems for which the dynamics can be described within a limited number of degrees of freedom. They are only valid at liquid helium temperatures when the lattice motion is quenched. Accordingly, as will be illustrated in measured spectra, tunnelling spectra are rather simple (see figures 2 and 3).

2.2. THE DYNAMICAL MATRIX FOR MOLECULAR VIBRATIONS

In contrast to tunnelling spectroscopy, vibrational spectra for most molecular systems are rather complex, there being $3n - 6$ non-zero modes for a molecule of n atoms. In a crystal with N atoms per unit cell, Bloch waves describe the modes, and $3N$ modes with wavevector $k = 0$, of which 3 translational (acoustic) modes have zero frequency, have to be calculated.